



Time-Dependant Microstructural Evolution and Tribological Behaviour of a 26 wt% Cr White Cast Iron Subjected to a Destabilization Heat Treatment

U. Pranav Nayak¹ · Frank Mücklich^{1,2} · María Agustina Guitar¹

Received: 17 March 2022 / Accepted: 10 July 2022
© The Author(s) 2022

Abstract

By employing destabilization heat treatments (HT), it is possible to create microstructures possessing different fractions of carbides, martensite, and austenite, which lead to varying tribological responses in abrasion-resistant high-chromium white cast irons. In the current work, the destabilization temperature was kept constant at 980 °C, whereas the time was varied from 0 to 90 min. As a result, the microstructure of the 26 wt% Cr white cast iron had a mixture of $M_{23}C_6$ secondary carbides (SC), martensite, and a decrease in the amount of retained austenite (RA) with increasing destabilization holding time. The microstructures as well as their tribological characteristics were evaluated by combining confocal laser scanning microscopy, SEM, XRD, and EBSD, together with dry-sliding linear reciprocating wear tests. Results show that the volume fraction of SC were statistically comparable in samples destabilized for 0 and 90 min, although the average size was almost two-fold in the latter. This had direct implications on the wear properties where a decrease of up to 50% in the wear rate of destabilized samples compared to the non-treated material was observed. Furthermore, the sample with the lowest increase in the matrix hardness (~20% higher than non-treated), showed the highest wear resistance. This was attributed to a favourable distribution of the RA (~10%) and SC volume fraction (~5%), in combination with the harder martensitic matrix. Finally, the results obtained from this study shed light on the ability to alter the HT parameters to tune the microstructure depending upon the application prerequisite.

Keywords High chromium cast iron · Destabilization heat treatment · Retained austenite · Secondary carbides · Wear rate · Microstructural tailoring

1 Introduction

Almost 25% of the world's energy production is spent in overcoming tribology-related issues [1]. Additionally, the friction and wear-related failures in the mining and mineral sector alone constitute for about 6% of the global energy consumption [2]. To reduce the energy and economic loss faced during operation run-time, scientists are constantly on the look out to develop better wear-resistant materials by understanding the wear mechanisms [3–5]. The application's

longevity can be extended by either employing new materials apt for wear-related applications or suitably modifying the existing material's microstructure.

High chromium white cast irons (HCWCIs) are alloys primarily belonging to the Fe–Cr–C ternary system, containing 15–30 wt% Cr and 2.4–4 wt% C (with additions of Ni, Cu, Mn and Mo), as described by the ASTM A532 [6, 7]. Their microstructure is characterized by the presence of Cr-rich M_7C_3 type carbides and a modifiable (ferrite, austenite, martensite) matrix. This combination of hard carbides (1200–1600 HV) dispersed in a versatile matrix enables it to be used in a wide variety of applications such as ore crushers, ball mill liners and pulverizing equipment, in the coal and mineral sector [7–10]. The versatility of the matrix stems from the ability to modify it by employing suitable heat treatments such as destabilization and/or sub-critical treatments [11, 12]. During destabilization, the precipitation of fine secondary carbides (SC) takes place, in addition to the transformation of the austenitic matrix to

✉ U. Pranav Nayak
pranav.nayak@uni-saarland.de

¹ Department of Materials Science, Saarland University, Campus D3.3, 66123 Saarbrücken, Germany

² Materials Engineering Center Saarland (MECS), Campus D3.3, 66123 Saarbrücken, Germany

martensite during cooling [7, 13]. Moreover, the characteristics of the SC are highly dependent on the destabilization specifics and the Cr/C ratio [14, 15].

Several works found in the literature evaluate the wear properties of HCWCI alloys as a result of varying the alloying elements [16–19] and heat treatment (HT) [11, 12, 20–23], where a strong correlation between the microstructural characteristics and wear resistance was observed. Although it was thought that a high hardness (i.e., maximum carbide precipitation and martensite formation) was the primary dictating factor for improving the wear resistance, it is now understood that a synergistic contribution between the carbide and matrix is key [4, 24]. This was evident in the studies carried out by Zum Gahr et. al. [25] and Doğan et. al. [26], wherein an increase in the hardness/carbide volume fraction (CVF) did not correspond to an increase in the wear resistance. Notwithstanding the contribution of the hard M_7C_3 carbides in improving the overall wear resistance of the HCWCI alloy, the degree of mechanical support provided by the matrix structure plays a crucial role [27, 28]. Furthermore, the stereological characteristics of the SC (size, type, volume fraction, etc.) may have an influence on the overall wear behaviour, as in the case of low-stress abrasion applications [29–31].

As far as the matrix structure is concerned, austenite in general is thought to provide good mechanical support to the carbides due to its ability to absorb the crack propagation and strain harden progressively during service [25, 32, 33]. Some studies indicate that the presence of retained austenite (RA) helps in improving the wear resistance by virtue of its inherent ductility [26, 32] and others suggest possessing a harder martensitic matrix might be the better option owing to the mechanical support it could provide [12, 22, 34–36]. Nevertheless, there is often conflicting information in the literature whether heat treatment modifications made to the as-cast hypoeutectic HCWCI alloy has improved the wear resistance or not. Additionally, numerous studies indicate a tendency of increasing wear resistance with increasing CVF when an abrasive softer than the M_7C_3 carbide is used, although there is no consensus among the community when the hardness of the abrasive (SiC/Al_2O_3) exceeds that of the carbide [3, 25], which elucidates the complexity associated with tribological testing [27]. Among a multitude of studies dealing with wear in cast irons, only a limited number of investigations dealt with sliding [19, 27, 37] and even fewer studies placed emphasis on the differential response of each individual microstructural constituent to the tribo-system after conducting dry-sliding wear tests [18, 38].

In the present work, an attempt was made to derive a mutual relationship between the volume fraction of RA, the stereological characteristics of SC precipitates and the matrix hardness of a 26 wt% Cr white cast iron, with the wear rate (WR), when destabilization holding time is increased. Subsequently, a destabilization HT was experimentally conducted wherein the samples were heated to 980 °C, held for various times ranging from 0 to 90 min, followed by air cooling. Microstructural characterization was performed on all the samples by confocal laser scanning microscopy (CLSM) and scanning electron microscopy (SEM). Additionally, the stereological characteristics of the SC precipitates were assessed in terms of volume fraction, size and near neighbour distance (nnd), and their respective distributions, by conducting image analysis on the SEM micrographs. To quantify the amount of RA present in heat-treated samples, X-ray diffraction measurements were combined with Rietveld analysis. The samples were later subjected to dry-sliding linear reciprocating wear tests to determine the wear volume loss and subsequently, the WR. Finally, SEM was used for the characterization of the wear tracks to correlate the improved wear resistance with the associated changes taking place during the destabilization treatment.

2 Experimental Methodology

2.1 Material and Heat Treatment

The bulk chemical composition (in wt%) of the HCWCI alloy used in the current work was determined by optical emission spectroscopy (GNR Metal Lab 75/80) and is presented in Table 1, whereas the specifics of the casting are mentioned in [39].

An abrasive disk was used to cut the cast samples measuring $20 \times 20 \times 10$ mm. Moreover, the smaller sample thickness ensures a quick thermal equilibration with the furnace and a uniform heating during the destabilization. Three samples were subjected to a destabilization heat treatment at 980 °C for 0 (Q_0), 30 (Q_30) and 90 (Q_90) minutes followed by air cooling and later, hot mounted in a conductive resin for metallographic preparation. The metallographic protocol as specified in [40] was followed to obtain a scratch-free, mirror polished surface. The schematic of the HT is represented in Fig. 1.

Table 1 Bulk chemical composition (wt%) of the HCWCI alloy used in this study

C	Cr	Mn	Ni	Mo	Si	Cu	P	S	Fe
2.53	26.60	0.66	0.26	0.24	0.37	0.03	<0.01	0.04	Bal

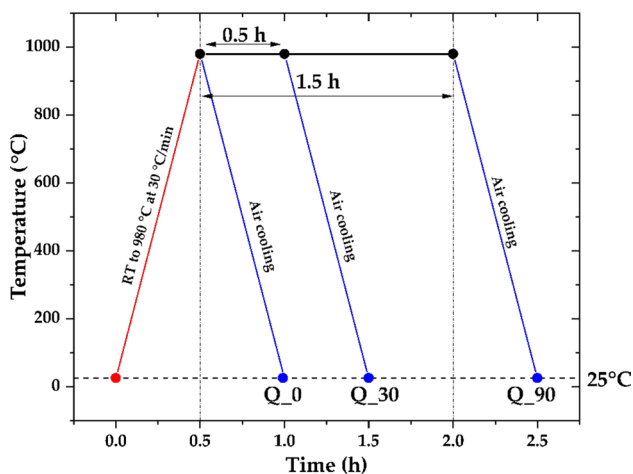


Fig. 1 Schematic of the destabilization heat treatment employed

2.2 Tribological Tests

Dry-sliding linear reciprocating wear tests were conducted on the as-cast (AC) and the HTed samples using a ball-on-disc micro-tribometer (CSM Instruments), while the whole setup was placed in an environmental chamber to control the temperature and humidity. 3 mm alumina (Al_2O_3) balls (99.00%–99.99% purity; Grade GD28) were used as the sliding counter-body. Table 2 represents the tribological testing parameters used during the test. Presently, a load of 20 N was used based on a previous work wherein the critical load was obtained using Hertzian contact theory based on the material that deforms first [41]. Moreover, at least three trials were performed for each sample.

2.3 Microstructural and Wear Track Characterization

Optical microscopy (OM) observations of the AC and HTed samples were carried out using a LEXT OLS 4100 Olympus CLSM. The CLSM uses a laser with 405 nm wavelength and, a lateral and vertical resolution of 120 and 10 nm, respectively. The fine microstructural details of the samples

Table 2 Tribological testing parameters

Parameters	Value
Temperature (°C)	25
Relative humidity (%)	45
Load (N)	20
Sliding velocity (ms^{-1})	0.02
Stroke length (mm)	5.5
No. of cycles	2000
Data acquisition frequency (Hz)	50

were obtained using a FEI Helios™ Nanolab 600 field emission SEM (FE-SEM) in conjunction with a Thermo-Fisher Helios™ G4 PFIB (Plasma Focused-Ion Beam) CXe DualBeam™ FIB/SEM. The SEM was operated at an acceleration voltage of 5–15 kV and a beam current of 1.4 nA. The AC microstructure is characterized by the presence of Cr-rich M_7C_3 type intergranular eutectic carbides (EC) (~30%) dispersed in an austenitic matrix (γ) (~60%), and a thin layer of martensite (α') (~10%) sandwiched between the EC and γ , as indicated in Fig. 2. The phases present in the microstructures are colour-arrow coded throughout the paper according to the following terminology:

Austenite (γ): Red arrow pointing downwards

Martensite (α'): Green arrow pointing upwards

M_7C_3 carbide (EC): Yellow arrow pointing right

M_{23}C_6 carbide (SC): Blue arrow pointing left

The back-scattered electron (BSE) micrographs obtained from the SEM were used in determining the stereological characteristics (volume fraction, size, and etc.) of the SC, using the open-source image analysis software, FIJI (Fiji Is Just ImageJ) [42]. Prior to obtaining the BSE SEM micrographs, the samples were etched with a modified Murakami's reagent (4 g $\text{K}_3[\text{Fe}(\text{CN})_6]$ potassium ferricyanide + 8 g NaOH sodium hydroxide + 100 mL H_2O water) at RT for 15 s [40]. The micrographs were captured at a magnification of $2500\times$ ($\sim 50 \times 50 \mu\text{m}^2$) and at least 5 micrographs were considered in each case. A threshold segmentation was applied to the BSE micrographs to obtain a binarized image comprising of the carbides and the matrix. This was followed by selectively eliminating the larger EC from the image and performing the particle analysis on the

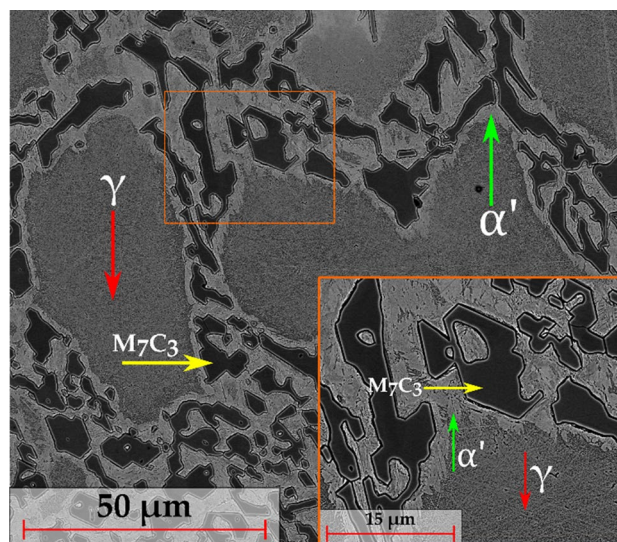


Fig. 2 Representative SEM micrograph of the AC sample after etching with Vilella's reagent. The various phases are marked for reference

SC. Considering the magnification and resolution of image acquisition, all pixelated particles having a diameter less than 100 nm were excluded from the analysis. Further details concerning the determination of the SC specifics is given in [43].

It was assumed that the carbide size and nnd's were log normally distributed as evidenced by the presence of skewness in the raw data. Moreover, an additional factor namely the coefficient of variation (COV) was introduced to measure the homogeneity of the SC distribution based on the log normal distribution data of the nnds [44, 45]. In Eq. (1), σ_{\ln} is the standard deviation of the nnd data after a natural log transformation. It is worth to note that lower the COV value, more homogeneous the sample data.

$$\text{COV} = \sqrt{e^{\sigma_{\ln}^2} - 1} \quad (1)$$

X-ray diffraction measurements of the AC and the HTed samples were carried out at room temperature using a PANalytical Empyrean diffractometer system equipped with a novel Bragg Brentano^{HD} module (to obtain a monochromatized divergent incident beam) and an ultra-fast PIXcel^{3D} detector (used in linear scanning mode). An X-ray tube with cobalt ($K\alpha = 0.1791$ nm) as the anode material was utilized as the radiation source along with a θ - 2θ scan geometry. The acceleration voltage and current applied during the measurements were 40 kV and 40 mA, respectively. The scans were made over a 2θ range of 40° to 130° with a step size of 0.013° and a counting time of 250 s, constituting a total scanning time of approximately 2 h. Moreover, the pulse height distribution settings were set to a range of 25.5% (3.53 keV)–80% (11.09 keV). The peak positions and phase identification was performed using the X'Pert High Score Plus software. Additionally, the volume fraction of the RA in the HTed samples was estimated by the Rietveld refinement approach [46], using the software Material Analysis Using Diffraction (MAUD) [47].

The matrix hardness was determined using the Vickers method using a Struers Dura Scan 50 microhardness tester with a load of 0.9807 N (HV0.1). During the testing, the dwell time was 15 s and the readings were averaged over 15–20 measurements. The load was chosen ensuring that the surrounding entities (EC and/or the interfacial α') are not participating in the evaluation of the matrix hardness and, the indentation mark was clearly resolvable using the optical microscope.

The morphological aspects of the wear tracks as well as the acting wear mechanisms were ascertained using CLSM and FE-SEM. A high-performance ion conversion and electron detector was employed during the SEM analysis to obtain a better phase contrast and emphasize on certain regions of interest within the wear track. Energy-dispersive

X-ray spectroscopy (EDS) was used to chemically map the worn and the unworn surface.

The local deformation and the strain distribution at the vicinity of the wear track was investigated by electron backscattered diffraction (EBSD). The measurements were performed at an acceleration voltage of 20 kV and a beam current of 11 nA, using the FE-SEM workstation equipped with an EDAX Hikari EBSD camera. The EBSD data was analysed using the Orientation Imaging Microscopy (OIMTM v. 7) Data Analysis software by EDAX Corporation. Kernel average misorientation (KAM) measurements were carried out to extract orientation data within the deformed regions. Owing to the very small step size (30–50 nm), 2nd neighbour KAM with a 5° threshold was considered for the analysis. Additionally, misorientation profile analysis was performed around the deformed region to obtain the orientational variation.

Wear quantification was described in terms of WR, and it was proceeded by calculating the volume loss encountered in each track using the proprietary LEXT software in the CLSM. The entire wear track, including the ends were considered in the calculations, and Eq. (2) was used to compute the WR, where V represents the wear volume (mm^3), l is the total sliding distance ($5.5 \times 2 \times 2000$ mm), P is the applied load (N), and WR represents the wear rate ($\text{mm}^3 \text{N}^{-1} \text{mm}^{-1}$).

$$\text{WR} = \frac{V}{l \times P} \quad (2)$$

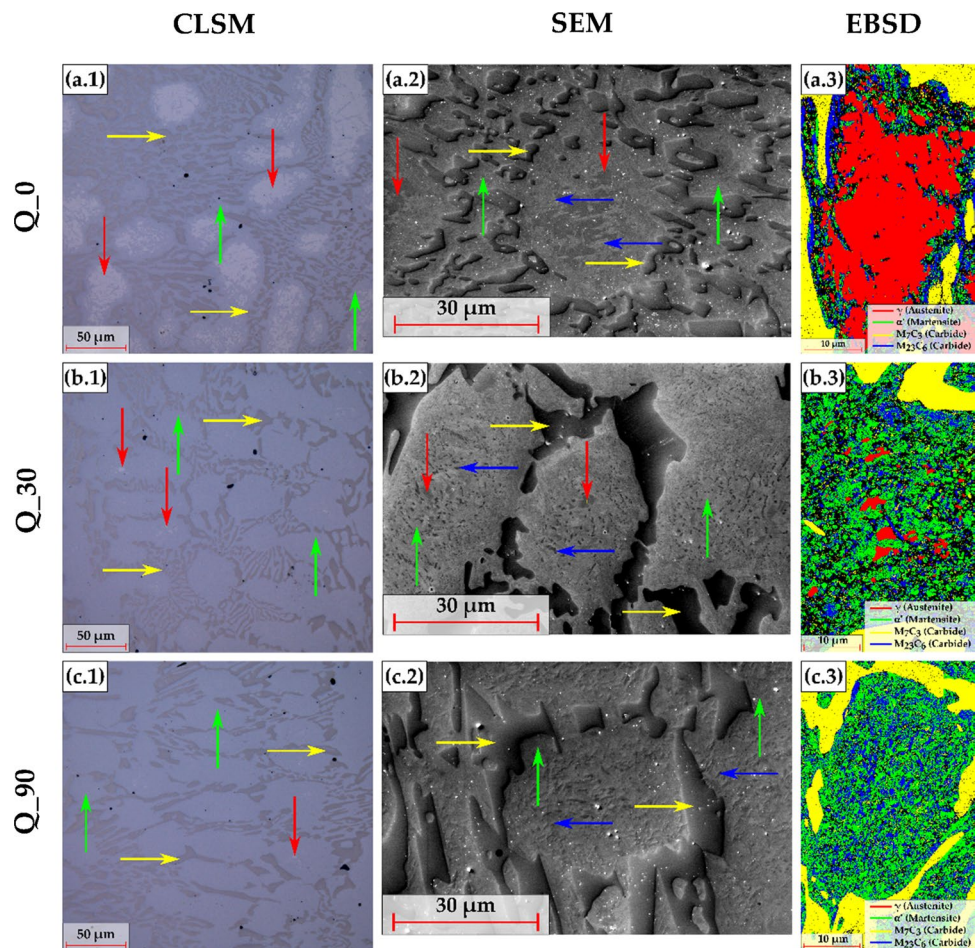
3 Results and Discussion

3.1 Microstructural Characterization of the Destabilized Samples

Figure 3 represents the micrographs obtained from CLSM and SEM, and the EBSD phase maps for the destabilized samples. The HTed microstructure is characterized by the presence of a primarily martensitic matrix (α'), finely precipitated SC ($M_{23}C_6$ type), the original (as-cast) EC (M_7C_3 type) and RA. The EC (in terms of volume fraction and size refinement) are relatively immune to the HT considering their thermal stability [7, 13, 48] and the destabilization temperature used in the present work. Hence, it is assumed that all the changes are taking place predominately in the matrix.

Comparing the CLSM micrographs (a.1, b.1 and c.1 in Fig. 3) of the HTed samples, a reduction in the RA content (white patches) was observed with increasing destabilization holding time. Moreover, the SEM micrographs (a.2, b.2 and c.2 in Fig. 3) give a visual perspective of the SC distribution throughout the material. In fact, the precipitation of SC and the reduction of RA is an interdependent process [11, 12].

Fig. 3 Micrographs of the destabilized samples obtained using CLSM (1) and SEM (2), and the EBSD phase maps (3), for Q_0 **a**, Q_30 **b** and Q_90 **c**, respectively. The phases are accordingly colour and arrow-labelled for reference



During destabilization, the increased driving force for alloy redistribution results in the precipitation of $M_{23}C_6$ type SC [49]. In the Q_0 sample, they are primarily located at the periphery of the matrix, whereas in the case of Q_30 and Q_90, they are also located within the body of the matrix. This indicates that the precipitation initially occurred at the periphery and proceeded inwards into the body of the matrix. This sequence was also observed in other studies [13, 14, 50, 51].

Additionally, the variation in the size and shape of the SC indicate that they may have precipitated at different times during the destabilization heat treatment. In a recent work, simulations using MatCalc predicted that precipitation started during heating at approximately 800 °C and additional precipitation took place during the initial cooling phase (980–750 °C) [49]. Considering the sample size used in the present work and the fact that it was kept inside the furnace during the heating, and not inserted once the intended destabilized temperature was reached, precipitation had taken place during the heating. Consequently, the stability of the austenite is reduced owing to the depletion in carbon, leading to a partial transformation to martensite upon cooling.

Furthermore, the EBSD phase maps (a.3, b.3 and c.3 in Fig. 3) of the matrix region indicate both the reduction in the RA with increasing destabilization holding time, and the distribution variation in the SC precipitates. Although the CLSM and SEM micrographs can be considered representative, it is worth to note that the EBSD phase map was obtained from a very small region and should be treated with caution. Nevertheless, the correlative microscopy (CLSM—SEM—EBSD) approach was very useful in the assessment of the destabilized microstructure.

The X-ray diffractograms of the AC and HTed samples are presented in Fig. 4a wherein the various phases are indexed for reference. Moreover, the 2θ values ranging from 51° to 54° (as indicated by the dashed-black enclosure in Fig. 4a) were subjected to peak deconvolution and fitting, as represented from Fig. 4b–e. A clear shoulder is seen for the AC sample which was separated into two individual peaks of M_7C_3 and α' using a pseudo-Voigt function. Comparing the most intense peak of the HTed samples i.e., the (110) martensite peak, a shift in the peak position is observed. The (110) α' peak in Q_0 is slightly shifted at a higher 2θ angle compared to the Q_30 and Q_90 which is an indication of lower carbon in the martensite phase. The presence of

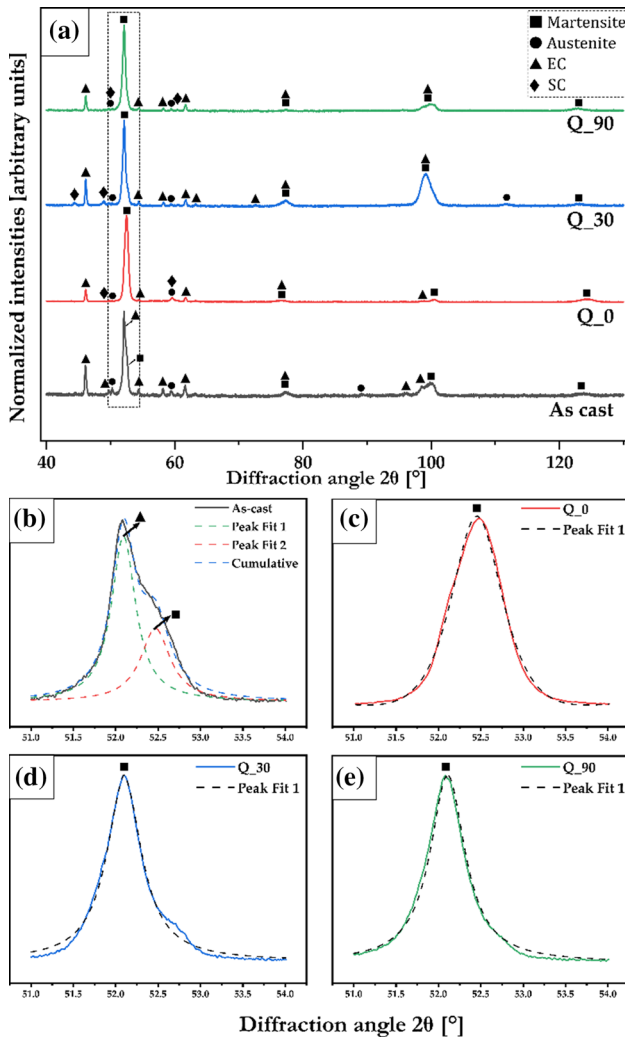


Fig. 4 a X-ray diffractograms of the AC and HTed samples. b–e represent a corresponding magnified view of the peaks and the associated peak deconvolution from 2θ values ranging from 51° to 54° , as indicated by the dashed black enclosure in a

a higher amount of carbon in the martensite lattice distorts it even more increasing the interplanar spacing. Considering the inverse relationship between the interplanar spacing and the Bragg's angle in the Bragg equation, this leads to a shift in the peak towards lower 2θ values which is observed in the X-ray diffractograms. Considering the similarity between the positions of the (110) α' peaks in Q_30 and Q_90, a larger lattice deformation compared to the Q_0 sample can be inferred, which should lead to a harder martensitic phase [52].

The calculated CVF (%) and average size (μm^2) of the SC are represented in Fig. 5. A decrease in the CVF is observed in the first 30 min and later, it increases from Q_30 to Q_90. The CVF values of Q_0 and Q_90 is statistically comparable, although the average size increased two-fold in the latter. Comparing Q_0 with the Q_30 sample, even though the

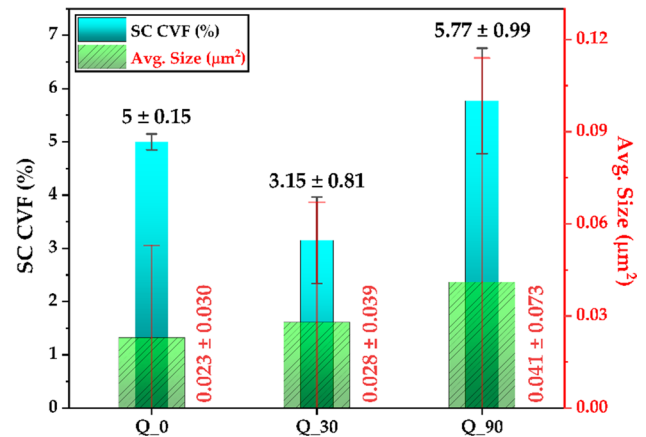


Fig. 5 The secondary carbide volume fraction (%) and the corresponding average size (μm^2) for the destabilized samples

CVF reduced ($\sim 40\%$), the average size remained within the tolerance interval ((Mean + S.D.)—(Mean—S.D.)). Additionally, the distribution of the SC in terms of size and nnd can also provide crucial information in understanding the precipitation specifics [7, 11, 51].

The log normal size distribution (in terms of particle count vs. area (μm^2)) for the three HTed samples is graphically represented in Fig. 6a. The average size for the corresponding samples is indicated in the inset table in Fig. 6a. The cumulative distribution curve is plotted in Fig. 6b which shows that for a given size, the percentage of particles falling within that size range decreases from Q_0 to Q_90. This is further exemplified by the distribution-rug plot in Fig. 6c, plotted on a log–log scale for better visualization, where it is indicated that the Q_90 sample possesses a higher number of particles with larger sizes, whereas the particle distribution between Q_0 and Q_30 is similar. Combining the information obtained from Fig. 6a concerning the reduction in particle count, with the rug plot in Fig. 6c, it is evident that the average size increases from Q_0 to Q_90.

As the precipitation takes place by nucleation and growth phenomena, they need to overcome a certain activation barrier to achieve a critical size to nucleate. Moreover, new phases tend to favour precipitating on heterogeneous surfaces such as defect clusters, sub-grain boundaries, etc., where it is thermodynamically more favourable [53, 54]. The fresh precipitation could be presumed to have taken place during two stages of the HT i.e., heating and cooling. During heating, the transformation of the interfacial martensite to austenite at the periphery results in the austenite possessing a large number of defects. This stems from the stresses generated owing to the differences in coefficient of thermal expansion between the hard M_7C_3 EC and the austenitic matrix. This generation of defect clusters at the periphery reduces the activation energy required to achieve the critical

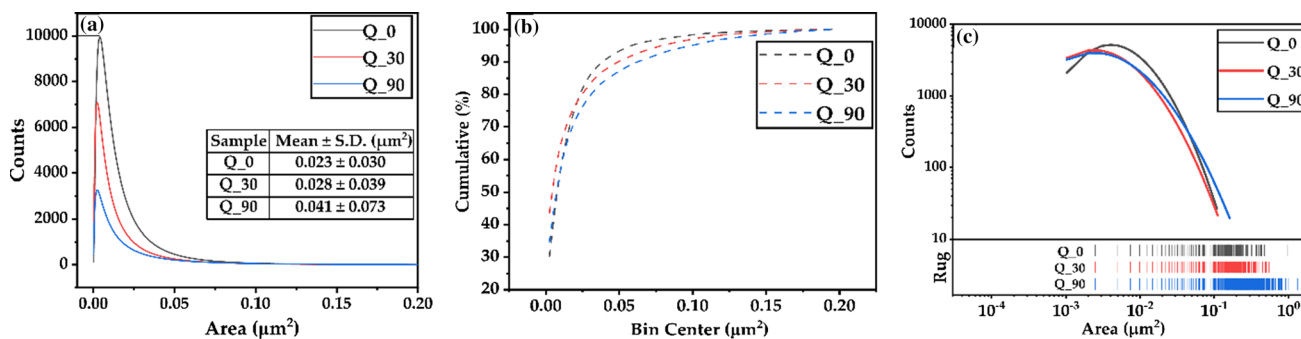


Fig. 6 a log normal size distribution of the SC for the HTed samples with the inset table representing the average size for each of the destabilized samples. The peak of the distribution curves signifies the corresponding modes. The cumulative distribution curve is plotted

in **b** and, **c** distribution-rug plot plotted on a log–log scale, which is indicative of a histogram with zero-width bins and used to visualise distribution of the data

size, resulting in a large number of small-sized carbides nucleating at those regions [48, 50]. Subsequently, some of the freshly precipitated carbides can also partially redissolve into the matrix. This can be thought to take place in the first 30 min (Q_0 → Q_30) wherein the particle count and CVF is decreasing with the average size remaining statistically within range, as indicated in Figs. 5 and 6. Simultaneously, the continuous alloy redistribution taking place during the isothermal holding results in the growth and coalescence (Ostwald ripening) of SC in other regions of the matrix. This is expected to take place from Q_30 → Q_90, as evident from Fig. 6, where the average size and CVF is increasing, and the number of particles is decreasing. Nevertheless, the presence of small-sized carbides at the periphery of all the HTed samples is indicative of the fact that additional precipitation took place during the cooling stage, but no time was given to facilitate their growth [49, 55].

The nnd distribution was also log normally plotted and is represented in Fig. 7a. The inset table in Fig. 7a indicates the mean nnd value for the three HTed samples, being the lowest for the Q_0 amongst all the conditions. Although the mean nnd values of the HTed samples fall within the tolerance

interval, analysing their distribution gives information on their homogeneity. Figure 7 (b) and Fig. 7c represent the nnd cumulative distribution curve and the nnd distribution-rug plot, respectively. The COV was determined for each of the HTed samples considering the standard deviation of the log normally distributed nnd values (σ_{ln}) and using Eq. (1). Sample Q_0 had a COV of about 40% whereas the Q_30 and Q_90 samples showed COV values of 49% and 47%, respectively. It also worth to mention that although the COV value of Q_0 is the lowest indicating that the dispersion of SC precipitates relatively more homogeneous, this should not be considered as the sole deciding factor. This approach fails to consider the fact that in the Q_0 sample, most of the precipitates are located around the periphery of the matrix and therefore, are considerably more closely spaced compared to the Q_30 and Q_90 samples. In the case of the Q_30 and Q_90 samples, the particles are also predominately present at the body of the matrix (Fig. 3). The slight increase in the COV value of Q_30/Q_90 could be explained by the dissolution of the carbides at the periphery and the presence of carbides in the matrix body, leading to a higher absolute average nnd value. This trend is also exemplified in the rug

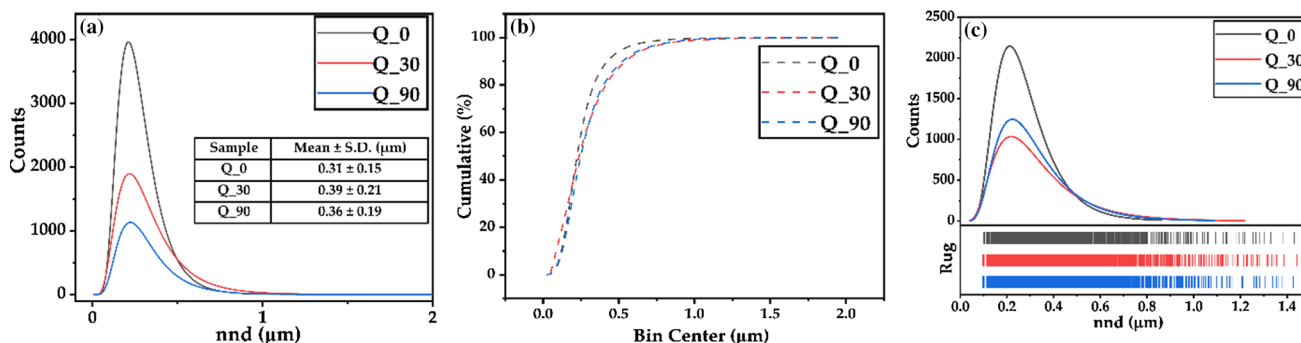


Fig. 7 a log normal near neighbour distance (nnd) distribution of the SC for the HTed samples with the inset table representing the average nnd for each of the destabilized samples. The cumulative distribution curve is plotted in **b** and, **c** distribution-rug plot plotted on a linear scale

plot in Fig. 7c) where the increased dispersion in the red vertical lines (Q_30) can be observed. The information obtained from the homogeneity calculations should also be combined with the size and nnd analysis to explain the changes taking place during the HT.

The estimation of the RA content in AC and HTed samples, along with the measured matrix hardness is given in Table 3. A clear trend is visible with respect to the RA content i.e., increasing the destabilization holding time results in the reduction of the RA, as also indicated by the correlative microscopy analysis of Fig. 3. Moreover, the implications of

the SC distribution and the associated $\gamma \rightarrow \alpha'$ matrix transformation on the hardness is evident. The presence of a large number of small-sized carbides located at the periphery of the matrix renders the central part of the matrix primarily austenitic, as observed from Fig. 3 (a.1) and Fig. 3 (a.3). As a result, the hardness of the Q_0 sample is increased marginally compared to the AC. With increasing holding time, the precipitation proceeds inwards into the matrix tending to grow and coalesce. This results in more of the austenite being transformed to martensite upon cooling and eventually a substantial increase in the matrix hardness, as evidenced from Table 3. Furthermore, it could be deduced from XRD that the martensite formed in the Q_30 and Q_90 samples is harder compared to the Q_0 owing to the shift in the (110) α' peak, contributing to the two-fold increase in the matrix hardness. The similarities in the hardness of the Q_30 and Q_90 could be attributed to the like nature and distribution of the microstructural constituents.

Table 3 The values of the retained austenite estimated using MAUD and the corresponding matrix hardness (HV0.1). The RA value of the As-cast was determined metallographically*, whereas Rietveld analysis by MAUD** was used for the HTed samples

Sample	Retained austenite (MAUD) (%)	Matrix hardness (HV0.1)
As-cast*	58.1	347 ± 24
Q_0**	10.2	412 ± 31
Q_30**	7.1	759 ± 22
Q_90**	5.1	775 ± 33

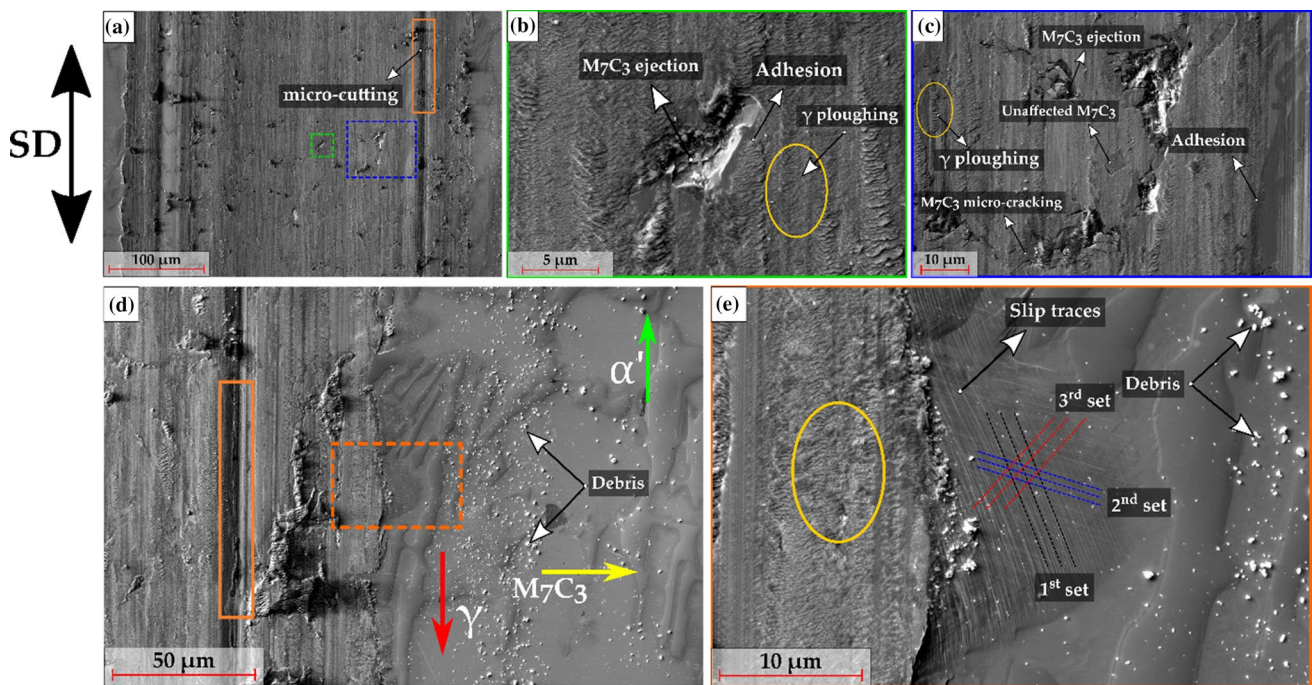


Fig. 8 a–c SEM secondary electron (SE) micrographs of the wear track for the AC sample with the various aspects of the wear track delineated and the corresponding magnified SE micrographs of the dashed-green and the dashed-blue areas. The γ , α' and M_7C_3 (EC) phases are marked in **d**, along with the wear debris. **e** SE micrograph of the dashed-orange enclosure marked in **d**. The slip traces, in addition to the three different sets of activated slip planes are indicated in **e**. The solid-orange enclosure and solid-yellow ellipse is indicative of the micro-cutting and austenite (γ) ploughing phenomena, respectively. The sliding direction (SD) is also mentioned for reference

tion to the three different sets of activated slip planes are indicated in **e**. The solid-orange enclosure and solid-yellow ellipse is indicative of the micro-cutting and austenite (γ) ploughing phenomena, respectively. The sliding direction (SD) is also mentioned for reference

3.2 Tribological Response of the AC and HTed Samples

3.2.1 As-Cast

Figure 8a–c represents the SEM SE micrograph encompassing the entire track width, together with the corresponding magnifications of the dashed-green and dashed-blue enclosures. From the micrographs, it was observed that the wear track had shown traits of adhesion especially at the matrix-carbide interface. Moreover, micro-cutting of the carbide and micro-ploughing of the austenite matrix (as evidenced by the presence of grooves bordered by lateral ridges), characteristic mechanisms of abrasive wear, was also observed. Figure 8d represents the SE SEM micrograph of the wear track with emphasis on the matrix region adjacent to the wear track and the corresponding magnified micrograph of the dashed-orange enclosure is depicted in Fig. 8e. Plastic deformation of the austenitic matrix can be observed, evidenced by the slip traces at the region adjoining the wear track, which are a manifestation to accommodate the deformation endured by the austenite. As a result of micro-cutting and micro-ploughing, cracking, and ejection of small fragments of EC ensue, as detailed in a previous work dealing with the analysis of the microstructural evolution of the AC

26 wt% Cr white cast iron under identical sliding conditions [41].

3.2.2 Destabilization for 0 min (Q_0)

The SEM SE micrographs of the Q_0 wear track is represented in Fig. 9. Two scenarios are depicted depending on whether the matrix adjacent to the wear track was martensite (Fig. 9a, b) or austenite (Fig. 9c, d). The presence of slip traces is a clear indication of the austenite deformation and is marked in Fig. 9c, d. On the contrary, no slip traces were observed when the martensite was adjacent to the wear track, owing to its inability to plastically deform considering the load used in the present study [41, 56]. The phenomenon of adhesion was observed, as in the AC condition, primarily at the matrix-carbide interface. The O EDS concentration map (Fig. 9e) indicates the preferential accumulation of oxides where the carbides have been cracked and/or ejected [41, 57].

Figure 10a represents the SEM SE micrograph of the area adjacent to the wear track edge where the EBSD measurements (dashed-blue enclosure) were carried out. The phase map in Fig. 10b clearly shows that the area adjacent to the wear track was primarily austenitic and the manifestation of slip bands is an indication of the austenite deformation, as marked by the dashed-orange enclosure in Fig. 10a. Comparing Fig. 10a, b, the slip lines terminate

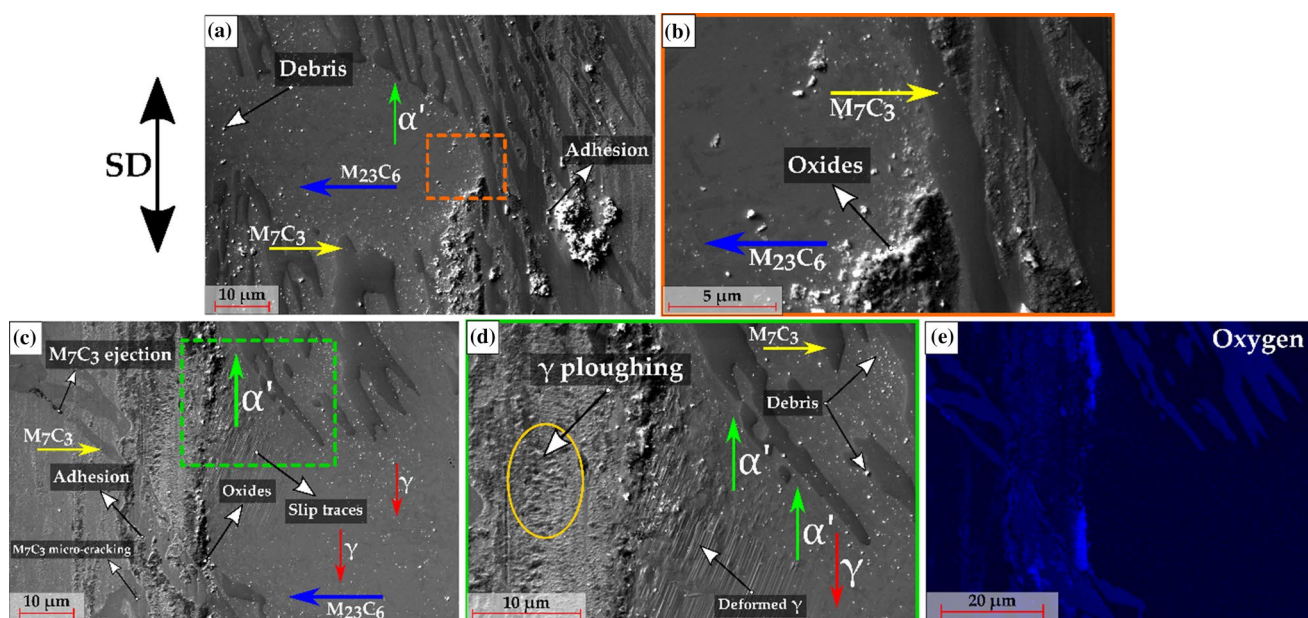


Fig. 9 **a** SEM SE micrograph of the wear track for the Q_0 sample when the matrix adjacent to the track is primarily martensitic. **b** magnified SE micrograph of the dashed-orange enclosure marked in **a**. **c** SEM SE micrograph of the wear track when the austenite phase is adjacent to the wear track, indicating the adhesion, carbide micro-

cracking and ejection. **d** magnified SEM micrograph of the dashed-green enclosure in **c**. The wear debris, the deformed austenite and ploughing effect is marked in **d**. **e** O EDS concentration maps of the micrograph presented in **c**. The SD is also mentioned for reference

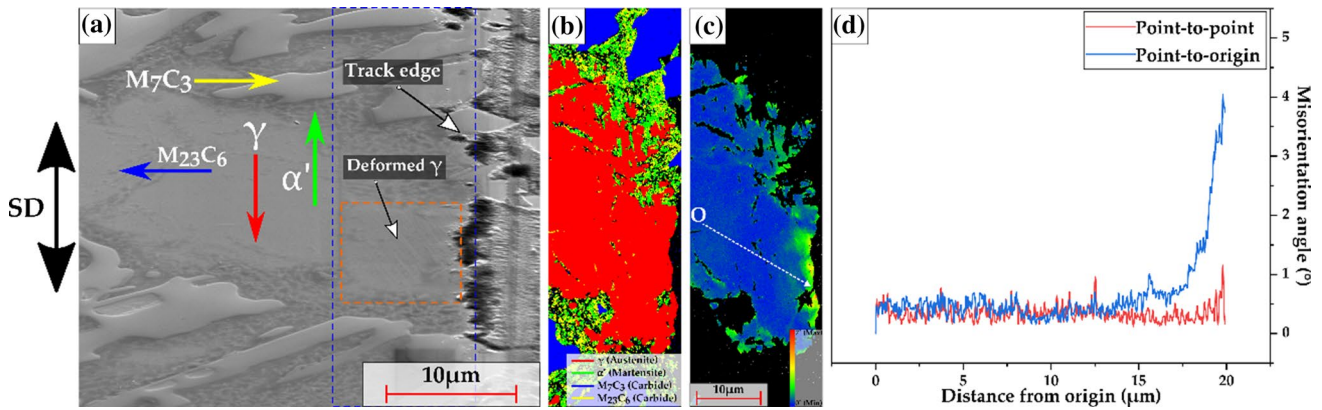


Fig. 10 **a** SEM SE micrograph of the wear track for the Q_0, with the various phases and the deformed γ delineated. **b** EBSD phase map of the dashed-blue enclosure in **a**, **c** KAM map of the austenite region. The variation of the misorientation angle (point-point and point-ori-

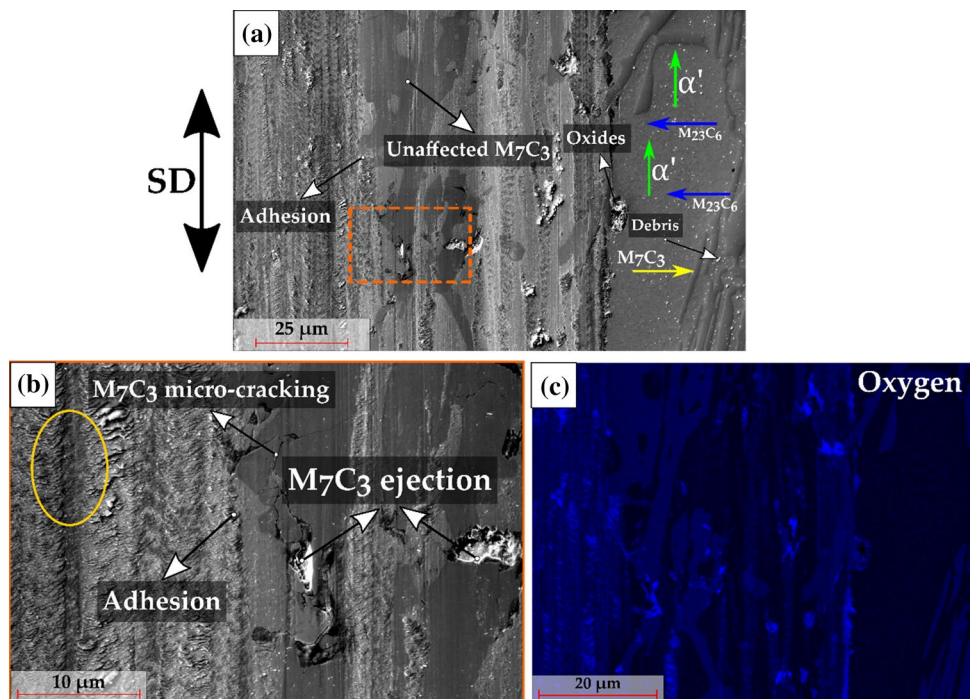
gin) across the austenite region starting from the point O following a path indicated by the dashed-white line in **c** is graphically represented in **d**. The SD is also marked for reference

upon encountering the martensite phase. This is attributable to the difference in crystal structure and a higher hardness. Figure 10c indicates the KAM map of the isolated austenite region. The orientational variation of the adjacent austenite region was exemplified by calculating the point-to-point and point-to-origin misorientation profile chart, as represented in Fig. 10d. A variation of about 4° was observed between the deformed and undeformed austenite region. This rotation of the austenite crystal lattice allows a quantitative evaluation of the local plastic deformation [58].

3.2.3 Destabilization for 30 min (Q_30)

Figure 11 represents the SEM SE micrograph of the Q_30 wear track with Fig. 11b indicating a magnified micrograph of the dashed-orange enclosure in Fig. 11a. Unlike the Q_0 sample where the region adjacent to the wear track could be either RA or martensite, the Q_30 sample had a predominately martensitic matrix, and no austenite was visible next to the wear track. Since the martensite is not able to undergo plastic deformation, no slip traces are visible next to the track. Moreover, as the hardness of the alumina counter body (~ 1500 HV) is higher than the

Fig. 11 **a** SEM SE micrograph of the wear track for the Q_30 sample, with the phases and various aspects of the wear track delineated. The wear debris, the oxides and the unaffected EC is marked in **a**. **b** magnified SE micrograph of the dashed-orange enclosure marked in **a**, wherein the phenomenon of adhesion along with the carbide micro-cracking and ejection is indicated. The O EDS concentration maps is indicated in **c** of the micrograph presented in **a**. The SD is also mentioned for reference



HCWCI material and/or the Cr-rich M_7C_3 carbide hardness (~ 1200 HV), the carbides are prone to micro-cracking [32, 33]. Additionally, the presence of the unaffected M_7C_3 carbide in Fig. 11a is an indication that not all carbides had undergone cracking. This could be attributed to the carbide's geometric orientation and the increased load-bearing capacity of the martensite [59–62]. Comparing the O EDS concentration maps of Q_0 (Fig. 9e) and Q_30 (Fig. 11c), it can be qualitatively appreciated that the latter possesses a greater area where oxides have accumulated throughout the wear track.

3.2.4 Destabilization for 90 min (Q_90)

The SEM SE micrographs of the Q_90 wear track and the O EDS map is represented in Fig. 12. No major differences were observed between the wear behaviour of Q_30 and the Q_90 sample. Similar to the Q_30 sample, the wear track had shown indications of adhesion, micro-cutting, and ploughing, as well as carbide spallation and ejection. From Fig. 12c, it was observed that the carbide cracking had taken place perpendicular to the sliding direction. This is a commonly observed phenomenon in HCWCIs in response to the tangential stresses acting during the sliding process, leading to brittle fracture [59, 60]. Moreover, the similarities in the values of the matrix hardness and RA are suggestive that the samples show a similar wear rate.

Although the microstructural constituents of the HTed samples are identical, the differences in their amounts and distribution had a consequence on the final tribological behaviour of the alloy. In the case of the samples possessing a higher amount of austenite (as-cast and Q_0), the wear mechanisms can be thought of a combination of mild adhesion and abrasion (as evident from the micro-cutting and ploughing) although, the influence of oxidation cannot be completely dismissed. Whereas, in the Q_30 and Q_90 samples, in addition to adhesion and abrasion, oxidation also plays a big role in the wear behaviour due to the detachment of secondary carbides from the matrix, as evident from the EDS concentration maps (Figs 11 and 12) and as seen further, the frictional behaviour.

3.2.5 Wear Rate and COF

The mutual dependence of the WR ($\text{mm}^3 \text{N}^{-1} \text{mm}^{-1}$) on the rest of the microstructural characteristics for all samples is graphically represented in Fig. 13a, and two major observations were made. Firstly, all the destabilized samples had shown a lower WR compared to the AC sample and secondly, a harder matrix did not necessarily guarantee a better wear resistance. Interestingly, the Q_0 sample with the lowest hardness among all the HTed samples, showed the lowest WR (i.e., highest wear resistance). Compared to the AC sample, the Q_0 showed a reduction of about 50%, whereas in the Q_30 and Q_90 samples, a decrease of up

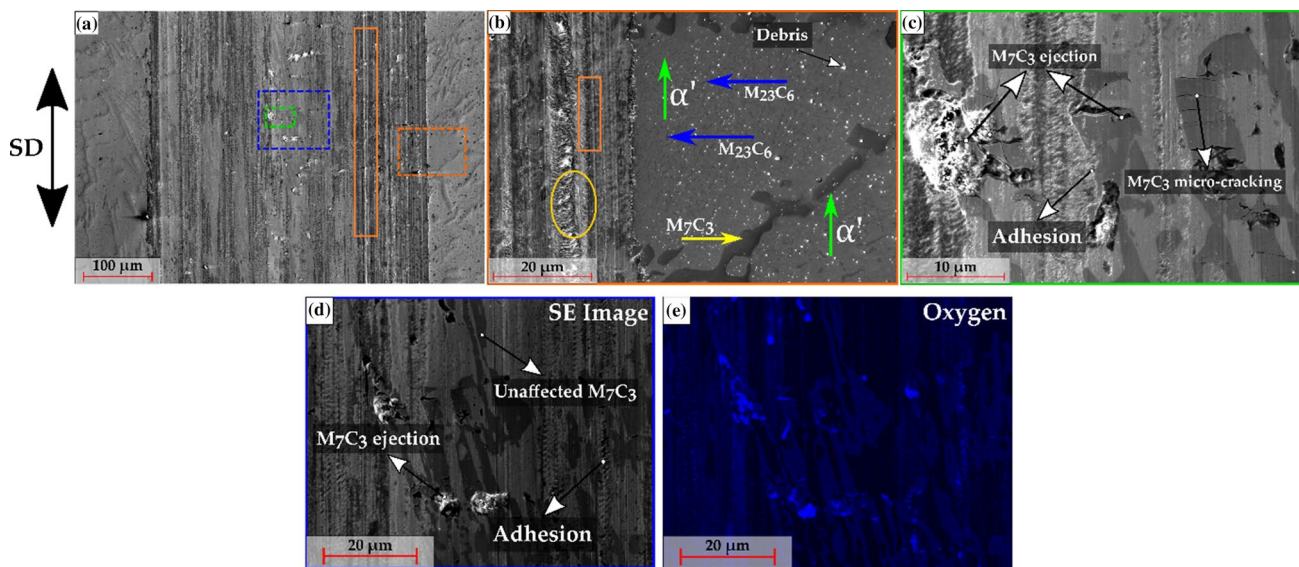


Fig. 12 **a** SEM SE micrograph of the wear track for the Q_90 sample, with the micro-cutting phenomenon delineated. The wear debris, the oxides and the unaffected EC is marked in **a**. **b** depicts the magnified SE micrograph of the dashed-orange enclosure marked in **a**, wherein the various phases, wear debris and the phenomenon of micro-cutting and ploughing is indicated. **c** magnified SE micrograph of the dashed-

green enclosure in **a** where the phenomenon of adhesion along with the carbide micro-cracking and ejection is visible. **d** A magnified SE micrograph of the dashed-blue enclosure in **a**. The EDS concentration maps of O is indicated in **e** of the micrograph presented in **d**. The SD is also mentioned for reference

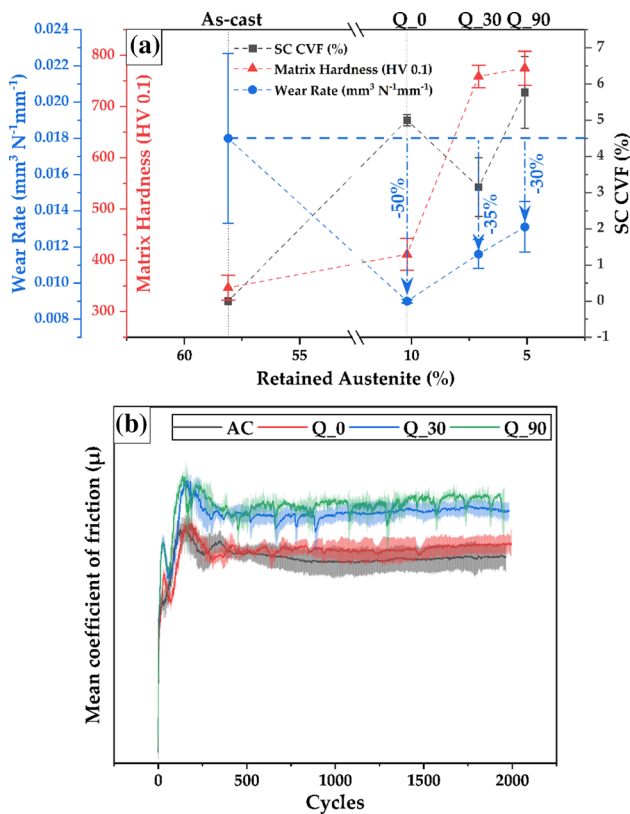


Fig. 13 **a** Graphical representation of the RA, WR, SC CVF (%) and matrix hardness (HV 0.1) values and **b** Mean coefficient of friction (COF) evolution for all the samples

to 35% was observed. Moreover, no major differences in the WR between the Q_30 and Q_90 samples were seen as hypothesized based on the microstructural characterization.

The frictional behaviour of the samples (expressed in terms of mean coefficient of friction (COF)) is represented graphically in Fig. 13b. In all cases, the curves reach a peak (running-in) before decreasing and reaching a steady state (SS). It is interesting to note that apart from the AC sample, all the HTed samples show a ‘double running-in’ behaviour. The initial peak is reached after about 75–100 cycles before showing a slight decrease after which it again ramps up to a higher peak value after about 250 cycles before settling at a SS value. The mean SS COF values of the AC and the Q_0 sample is comparable whereas the corresponding values of Q_30 and Q_90 are similar, indicating a distinction between the two groups. The main distinguishing feature is the presence of a relatively higher percentage of austenite in the AC and Q_0 sample compared to the latter two. In the Q_0 sample, the relatively higher amount of austenite could be thought to have provided additional mechanical support to the surrounding carbides by undergoing plastic deformation during the wear test. This was evident in Figs. 9 and 10

where the slip lines are visible emanating from the austenite region. In the Q_30 and Q_90 samples, the predominately martensitic matrix is unable to plastically deform compared to the austenitic matrix and thus incapable of providing the necessary support for its surrounding carbides leading to carbide micro-fracture and eventual ejection. The increased carbide ejection results in an increasing number of voids allowing the oxide to accumulate in those regions and further influence the wear behaviour [41]. This can be appreciated in the steady state behaviour of the Q_30 and Q_90 samples, wherein the continuous fluctuations indicate the formation and breakage of the oxide layer [63]. Although these fluctuations stop after about 1000 cycles for the Q_30 sample indicating conformity has reached, they continue for the Q_90 sample for the whole duration of the wear test.

As the matrix is worn out by the abrasive process, the support it offers to the carbides dwindles, resulting in an increased abrasive wear volume loss [64]. In the Q_90 sample, even though the CVF is comparable to that of the Q_0 sample, the decreased amount of RA and the increase in the average carbide size led to a higher probability of SC being ejected, leading to a change in wear mechanism towards oxidative wear and an increase in the WR. A decrease in the average carbide size for a constant carbide volume shortens the mean distance between the carbides, thereby minimizing the matrix exposure to contact damage [31].

Another factor for the lower WR of the HTed samples compared to the AC could be attributed to the cracking of the large EC. It was markedly higher in the AC sample compared to the HTed samples. Although the M_7C_3 type of EC has a higher inherent fracture toughness, the assumption that the EC are unaffected during the heat treatment implies the reduced prevalence of cracking is due to the changes taking place in the matrix during destabilization. This could be attributed to the presence of the hard martensite which improves the load-bearing capacity, thereby reducing the tendency for carbide micro-fracture [12, 29]. Additionally, the varying size distributions of the finely dispersed SC led to smaller SC particles participating in the intermixing of the tribologically transformed zone whereas the larger particles assisted in distributing the load. Although at higher destabilization holding times, the increasing average size of the SC made its ejection more probabilistic, especially with a martensitic matrix surrounding it. This led to the wear mechanism tilting in favour of oxidation, negatively impacting the WR. Nevertheless, the presence of a harder martensitic matrix and the distribution of SC throughout the HTed samples ensured an increased wear resistance compared to the AC sample.

4 Conclusions

In the current study, dry sliding linear-reciprocating wear tests were performed on a destabilized 26 wt% Cr white cast iron. The effect of increasing the destabilization holding time on the microstructural evolution and the subsequent tribological behaviour of the alloy was examined and the following conclusions were drawn.

- Microstructural observations revealed that destabilization resulted in the precipitation of fine SC and a temporal increase in the transformation of austenite to martensite, whereas the EC remained relatively immune to the HT.
- Stereological characterization of SC indicated a decrease in the CVF in the first 30 min and later, an increase from Q_30 to Q_90. The CVF values of Q_0 and Q_90 is statistically comparable, although the average size increased two-fold in the latter.
- The matrix hardness of the HTed samples increased up to 125% compared to the AC sample (owing to the presence of SC and a martensitic matrix) although, there was no significant rise between the Q_30 and Q_90 sample, indicating stagnation.
- All the HTed samples showed a reduction in the WR compared to the AC sample, with the Q_0 sample presenting the highest reduction (50%).
- The Q_0 sample showed the lowest WR, even though it did not present the highest matrix hardness among all the samples. This sheds light on the importance of an optimal distribution between the microstructural constituents after destabilization.
- Selection of the right heat treatment is highly dependent on the intended application. Samples Q_30 or Q_90 could be chosen if having a high hardness is a prerequisite as both the samples show a hardness of about twice that of the Q_0 sample. Hence, for applications where a high hardness is a requirement, it is recommended to destabilize for a longer period to ensure the amount of RA is reduced whereas for wear resistant applications, the presence of ~10% RA in addition to the precipitated SC (~5%) is advantageous.

Acknowledgements The present work is supported by funding from the Deutsche Forschungsgemeinschaft (DFG, project: GU 2102/2-1). The authors would like to thank the Saarland State Chancellery for financial support within the ZuMat Project funded by the European Regional Development Fund (ERDF). Moreover, the funding for the PFIB/SEM instrument by DFG is greatly acknowledged (INST 256/510-1 FUGG). The authors would also like to thank Martin Duarte from Tubacero S.A. for providing the materials and finally, U.P.N. is grateful to DAAD for the financial support.

Funding Open Access funding enabled and organized by Projekt DEAL.

Declarations

Conflict of interest The authors declare that they have no conflict of interest.

Open Access This article is licensed under a Creative Commons Attribution 4.0 International License, which permits use, sharing, adaptation, distribution and reproduction in any medium or format, as long as you give appropriate credit to the original author(s) and the source, provide a link to the Creative Commons licence, and indicate if changes were made. The images or other third party material in this article are included in the article's Creative Commons licence, unless indicated otherwise in a credit line to the material. If material is not included in the article's Creative Commons licence and your intended use is not permitted by statutory regulation or exceeds the permitted use, you will need to obtain permission directly from the copyright holder. To view a copy of this licence, visit <http://creativecommons.org/licenses/by/4.0/>.

References

1. K. Holmberg, A. Erdemir, *Friction* **5**, 263 (2017). <https://doi.org/10.1007/s40544-017-0183-5>
2. K. Holmberg, P. Kivikytö-Reponen, P. Härkisaari, K. Valtonen, A. Erdemir, *Tribol. Int.* **115**, 116 (2017). <https://doi.org/10.1016/j.triboint.2017.05.010>
3. J.D. Watson, P.J. Mutton, I.R. Sare, *Met. forum* **3**, 74 (1980)
4. K.H. Zum Gahr, D.V. Doane, *Metall. Trans. A* **11**, 613 (1980). <https://doi.org/10.1007/BF02670698>
5. C.G. Oliveira, I.P. Pinheiro, *MRS Online Proceedings Library* **1816**, 65 (2016). <https://doi.org/10.1557/opl.2016.65>
6. ASTM A532/A532M-93a, Standard Specification for Abrasion Resistance Cast Irons (ASTM International, West Conshohocken, 2003)
7. C.P. Tabrett, I.R. Sare, M.R. Ghomashchi, *Int. Mater. Rev.* **41**, 59 (1996). <https://doi.org/10.1179/095066096790326075>
8. R.J. Llewellyn, S.K. Yick, K.F. Dolman, *Wear* **256**, 592 (2004). <https://doi.org/10.1016/j.wear.2003.10.002>
9. E. Karantzalis, A. Lekatou, H. Mavros, *Int. J. Cast. Met. Res.* **22**, 448 (2009). <https://doi.org/10.1179/174313309X436637>
10. F. Maratray, *AFS Trans.* **79**, 121 (1971)
11. A.E. Karantzalis, A. Lekatou, H. Mavros, *J. Mater. Eng. Perform.* **18**, 174 (2009). <https://doi.org/10.1007/s11665-008-9285-6>
12. M.A. Guitar, S. Suárez, O. Prat, M.D. Guigou, V. Gari, G. Pereira, F. Mücklich, *J. Mater. Eng. Perform.* **27**, 3877 (2018). <https://doi.org/10.1007/s11665-018-3347-1>
13. H. Gasan, F. Erturk, *Metall. Mater. Trans. A* **44**, 4993 (2013). <https://doi.org/10.1007/s11661-013-1851-3>
14. G.L.F. Powell, G. Laird, *J. Mater. Sci.* **27**, 29 (1992). <https://doi.org/10.1007/BF02403640>
15. A. Wiengmoon, T. Chairuangri, J.T.H. Pearce, *ISIJ Int.* **44**, 396 (2004). <https://doi.org/10.2355/isijinternational.44.396>
16. R. Correa, A. Bedolla-Jacuinde, J. Zuno-Silva, E. Cardoso, I. Mejía, *Wear* **267**, 495 (2009). <https://doi.org/10.1016/j.wear.2008.11.009>
17. E. Cortés-Carrillo, A. Bedolla-Jacuinde, I. Mejía, C.M. Zepeda, J. Zuno-Silva, F.V. Guerra-Lopez, *Wear* **376–377**, 77 (2017). <https://doi.org/10.1016/j.wear.2017.02.043>
18. A. Bedolla-Jacuinde, R. Correa, I. Mejía, J.G. Quezada, W.M. Rainforth, *Wear* **263**, 808 (2007). <https://doi.org/10.1016/j.wear.2006.12.011>

19. C. Scandian, C. Boher, J.D.B. de Mello, F. Rézai-Aria, *Wear* **267**, 401 (2009). <https://doi.org/10.1016/j.wear.2008.12.095>
20. H. Gasan, F. Erturk, *Metall. Mater. Trans. A* **44**, 4993 (2013). <https://doi.org/10.1007/s11661-013-1851-3>
21. K.A. Kibble, J.T.H. Pearce, *Cast. Met.* **6**, 9 (1993). <https://doi.org/10.1080/09534962.1993.11819121>
22. C.P. Tabrett, I.R. Sare, *Scripta Mater.* **38**, 1747 (1998). [https://doi.org/10.1016/S1359-6462\(98\)00118-3](https://doi.org/10.1016/S1359-6462(98)00118-3)
23. A. Wiengmoon, T. Chairuangsi, J.T.H. Pearce, *Key Eng. Mater.* **658**, 76 (2015). <https://doi.org/10.4028/www.scientific.net/KEM.658.76>
24. J. Asensio, J.A. Pero-Sanz, J.I. Verdeja, *Mater. Charact.* **49**, 83 (2002). [https://doi.org/10.1016/S1044-5803\(02\)00260-7](https://doi.org/10.1016/S1044-5803(02)00260-7)
25. K.-H. Zum Gahr, G.T. Eldis, *Wear* **64**, 175 (1980). [https://doi.org/10.1016/0043-1648\(80\)90101-5](https://doi.org/10.1016/0043-1648(80)90101-5)
26. Ö.N. Doğan, J.A. Hawk, G. Laird, *Metall. Mater. Trans. A* **28**, 1315 (1997). <https://doi.org/10.1007/s11661-997-0267-3>
27. G. Laird, R. Gundlach, K. Rohrig, *Abrasion-Resistant Cast Iron Handbook* (American Foundry Society, Schaumburg, Illinois (USA), 2000)
28. H.S. Avery, *Wear* **4**, 427 (1961). [https://doi.org/10.1016/0043-1648\(61\)90301-5](https://doi.org/10.1016/0043-1648(61)90301-5)
29. S. Inthidech, Y. Matsubara, *Mater. Trans.* **49**, 2322 (2008). <https://doi.org/10.2320/matertrans.MRA2008079>
30. J.K. Fulcher, T.H. Kosel, N.F. Fiore, *Wear* **84**, 313 (1983). [https://doi.org/10.1016/0043-1648\(83\)90272-7](https://doi.org/10.1016/0043-1648(83)90272-7)
31. C. Rodenburg, W.M. Rainforth, *Acta Mater.* **55**, 2443 (2007). <https://doi.org/10.1016/j.actamat.2006.11.039>
32. R.B. Gundlach, J.L. Parks, *Wear* **46**, 97 (1978). [https://doi.org/10.1016/0043-1648\(78\)90113-8](https://doi.org/10.1016/0043-1648(78)90113-8)
33. J.T.H. Pearce, *Trans. Am. Foundrymen's Soc.* **92**, 599 (1984)
34. O.F. Higuera-cobos, F.-D. Dumitru, D.H. Mesa-Grajales, *Rev. Fac. Ing.* **25**, 93 (2016). <https://doi.org/10.19053/01211129.4141>
35. S. Inthidech, P. Kosasu, S. Yotee, Y. Matsubara, *Mater. Trans.* **54**, 28 (2013). <https://doi.org/10.2320/matertrans.M2012185>
36. K. Abdel-Aziz, M. El-Shennawy, A.A. Omar, *Int. J. Appl. Eng. Res.* **12**, 4675 (2017)
37. G. Pintaude, F.G. Bernardes, M.M. Santos, A. Sinatora, E. Albertin, *Wear* **267**, 19 (2009). <https://doi.org/10.1016/j.wear.2008.12.099>
38. S. Turenne, F. Lavallée, J. Masounave, *J. Mater. Sci.* **24**, 3021 (1989). <https://doi.org/10.1007/BF02385662>
39. U.P. Nayak, M.A. Guitar, F. Mücklich, *Metals* **10**, 30 (2020). <https://doi.org/10.3390/met10010030>
40. U.P. Nayak, M.A. Guitar, F. Mücklich, *Pract. Metallogr.* **57**, 688 (2020). <https://doi.org/10.3139/147.110682>
41. U.P. Nayak, S. Suárez, V. Pesnel, F. Mücklich, M.A. Guitar, *Friction* **10**, 1258 (2022). <https://doi.org/10.1007/s40544-021-0553-x>
42. J. Schindelin, I. Arganda-Carreras, E. Frise, V. Kaynig, M. Longair, T. Pietzsch, S. Preibisch, C. Rueden, S. Saalfeld, B. Schmid, J.-Y. Tinevez, D.J. White, V. Hartenstein, K. Eliceiri, P. Tomancak, A. Cardona, *Nat. Methods* **9**, 676 (2012). <https://doi.org/10.1038/nmeth.2019>
43. U.P. Nayak, M. Müller, D. Britz, M.A. Guitar, F. Mücklich, *Pract. Metallogr.* **58**, 484 (2021). <https://doi.org/10.1515/pm-2021-0039>
44. E. Limpert, W.A. Stahel, M. Abbt, *BioScience* **51**, 341 (2001). [https://doi.org/10.1641/0006-3568\(2001\)051\[0341:LNDATS\]2.0.CO;2](https://doi.org/10.1641/0006-3568(2001)051[0341:LNDATS]2.0.CO;2)
45. N. Yang, J. Boselli, I. Sinclair, *J. Microsc.* **201**, 189 (2001). <https://doi.org/10.1046/j.1365-2818.2001.00766.x>
46. H.M. Rietveld, *J. Appl. Crystallogr.* **2**, 65 (1969). <https://doi.org/10.1107/s0021889869006558>
47. L. Lutterotti, *Nucl. Instrum. Methods Phys. Res. Sect. B* **268**, 334 (2010). <https://doi.org/10.1016/j.nimb.2009.09.053>
48. A. Bedolla-Jacuinde, L. Arias, B. Hernández, *J. Mater. Eng. Perform.* **12**, 371 (2003). <https://doi.org/10.1361/105994903770342881>
49. M.A. Guitar, U.P. Nayak, D. Britz, F. Mücklich, *Int. J. Metalcast.* **14**, 755 (2020). <https://doi.org/10.1007/s40962-020-00407-4>
50. V.G. Efremenko, Y.G. Chabak, M.N. Brykov, *J. Mater. Eng. Perform.* **22**, 1378 (2013). <https://doi.org/10.1007/s11665-012-0434-6>
51. J. Ohser, F. Mücklich, *Statistical Analysis of Microstructures in Materials Science*, 1st edn. (Wiley, Hoboken, 2000)
52. B.D. Cullity, S.R. Stock, *Elements of X-Ray Diffraction*, 3rd edn. (Pearson Education, London, 2001)
53. D.A. Porter, K.E. Easterling, M.Y. Sherif, *Phase Transformations in Metals and Alloys*, 3rd edn. (CRC Press, Boca Raton, 2009)
54. X.Y. Liu, *J. Chem. Phys.* **112**, 9949 (2000). <https://doi.org/10.1063/1.481644>
55. J. Wang, C. Li, H. Liu, H. Yang, B. Shen, S. Gao, S. Huang, *Mater. Charact.* **56**, 73 (2006). <https://doi.org/10.1016/j.matchar.2005.10.002>
56. R. Abbaschian, L. Abbaschian, R.E. Reed-Hill, *Physical Metallurgy Principles*, 4th edn. (Cengage Learning, Stamford, 2009)
57. A. Bedolla-Jacuinde, W.M. Rainforth, *MRS Online Proceedings Library* **843**, 74 (2005). <https://doi.org/10.1557/proc-843-t7.4>
58. C. Schayes, J. Bouquerel, J.-B. Vogt, F. Palleschi, S. Zaefferer, *Mater. Charact.* **115**, 61 (2016). <https://doi.org/10.1016/j.matchar.2016.03.020>
59. J.J. Coronado, *Wear* **270**, 823 (2011). <https://doi.org/10.1016/j.wear.2011.02.009>
60. Ö.N. Doğan, J.A. Hawk, *Wear* **189**, 136 (1995). [https://doi.org/10.1016/0043-1648\(95\)06682-9](https://doi.org/10.1016/0043-1648(95)06682-9)
61. M. Jokari-Sheshdeh, Y. Ali, S.C. Gallo, W. Lin, J.D. Gates, *Wear* **492–493**, 204208 (2022). <https://doi.org/10.1016/j.wear.2021.204208>
62. J.J. Penagos, F. Ono, E. Albertin, A. Sinatora, *Wear* **340–341**, 19 (2015). <https://doi.org/10.1016/j.wear.2015.03.020>
63. P.J. Blau, *Tribol. Int.* **38**, 1007 (2005). <https://doi.org/10.1016/j.triboint.2005.07.020>
64. Y. Sano, T. Hattori, M. Haga, *ISIJ Int.* **32**, 1194 (1992). <https://doi.org/10.2355/ISIJINTERNATIONAL.32.1194>

Publisher's Note Springer Nature remains neutral with regard to jurisdictional claims in published maps and institutional affiliations.